6242 *Inorg. Chem.* **2009**, *48*, 6242–6250
DOI: 10.1021/ic900565m

Inorganic Chemistry
Article

Microstructures, Surface Properties, and Topotactic Transitions of Manganite Nanorods

Tao Gao,*,† Frank Krumeich,‡ Reinhard Nesper,‡ Helmer Fjellvåg,† and Poul Norby†

†*Centre for Materials Science and Nanotechnology and Department of Chemistry, University of Oslo, P.O. Box 1033, N-0315 Oslo, Norway, and* ‡*Laboratory of Inorganic Chemistry, ETH Zurich, Wolfgang-Pauli-Strasse 10, 8093 Zürich, Switzerland*

Received March 23, 2009

Manganite (γ−MnOOH) nanorods with typical diameters of 20−500 nm and lengths of several micrometers were prepared by reacting $KMnO_4$ and ethanol under hydrothermal conditions. Synchrotron X-ray diffraction (XRD) reveal that the γ−MnOOH nanorods crystallize in the monoclinic space group $P2_1/c$ with unit cell dimensions a = 5.2983(3) Å, b = 5.2782(2) Å, c = 5.3067(3) Å, and β = 114.401(2)°. Transmission electron microscopy shows that the γ−MnOOH nanorods are single crystalline and that lateral attachment occurs for primary rods elongated along ⟨101⟩. X-ray photoelectron spectroscopy studies indicate that the surfaces of the γ−MnOOH nanorods are hydrogen deficient and compensated by surface complexation. The Raman scattering spectrum features five main contributions at 360, 389, 530, 558, and 623 cm^{-1} along with four weak ones at 266, 453, 492, and 734 cm^{-1}, attributed to Mn−O vibrations within MnO_6 octahedral frameworks. The structural stability of the γ−MnOOH nanorods was discussed by means of in situ time-resolved synchrotron XRD. The monoclinic γ−MnOOH nanorods transform into tetragonal β−MnO_2 upon heating in air at about 200 °C. The reaction is topotactic and shows distinctive differences from those seen for bulk counterparts. A metastable, intermediate phase is observed, possibly connected with hydrogen release via the interstitial (1 × 1) tunnels of the γ−MnOOH nanorods.

Introduction

In natural environment, manganese oxides/hydroxides are found as several polymorphs with Mn in various oxidation states (2^+, 3^+ and 4^+).[1,2] Among these, Manganite, γ−MnOOH, is the most stable polymorph of the trivalent hydroxide and has important technological applications.[3−11] For example, γ−MnOOH has extraordinary adsorption capacities for scavenging numerous trace elements from aquatic environments.[3−5] γ−MnOOH is recognized for its strong oxidizing abilities for natural and xenobiotic organic substances and is a model compound in understanding reactivity of trivalent Mn in many minerals.[6−8] γ−MnOOH is an important precursor for the synthesis of complex Mn oxides, for example, Li−Mn−O[9] for lithium ion batteries.[10,11]

The synthesis of γ−MnOOH as nanowires/nanorods[12−20] attracts great interest because its properties are significantly modified when turning to nanometer-sized crystallites and

*To whom correspondence should be addressed. E-mail: tao.gao@kjemi.uio.no.

(1) Bricker, O. *Am. Mineral.* **1965**, *50*, 1296–1354.
(2) Post, J. E. *Proc. Natl. Acad. Sci. U.S.A.* **1999**, *96*, 3447–3454.
(3) McKenzie, R. M. *Aust. J. Soil Res.* **1980**, *18*, 61–73.
(4) Bochatay, L.; Persson, P.; Sjöberg, S. *J. Colloid Interface Sci.* **2000**, *229*, 584–592.
(5) Chiu, Van Q.; Hering, J. G. *Environ. Sci. Technol.* **2000**, *34*, 2029–2034.
(6) Stone, A. T. *Environ. Sci. Technol.* **1987**, *21*, 979–988.
(7) Mcardell, C. S.; Stone, A. T.; Tian, J. *Environ. Sci. Technol.* **1998**, *32*, 2923–2930.
(8) Ulrich, H. J.; Stone, A. T. *Environ. Sci. Technol.* **1989**, *23*, 421–428.
(9) Yang, X.; Tang, W.; Kanoh, H.; Ooi, K. *J. Mater. Chem.* **1999**, *9*, 2683–2690.
(10) Williams, G. R.; Norquist, A. J.; O'Hare, D. *Chem. Mater.* **2006**, *18*, 3801–3807.
(11) Li, X. D.; Yang, W. S.; Zhang, S. C.; Evans, D. G.; Duan, X. *Solid State Ionics* **2005**, *176*, 803–811.
(12) Du, G. H.; Yuan, Z. Y.; Van Tendeloo, G. *Appl. Phys. Lett.* **2005**, *86*, 063113 (3 pages).
(13) Yuan, Z. Y.; Ren, T. Z.; Du, G. H.; Su, B. L. *Appl. Phys. A: Mater. Sci. Process.* **2005**, *80*, 743–747.
(14) Yang, R.; Wang, Z.; Dai, L.; Chen, L. *Mater. Chem. Phys.* **2005**, *93*, 149–153.
(15) Folch, B.; Larionova, J.; Guari, Y.; Guérin, C.; Reibel, C. *J. Solid State Chem.* **2005**, *178*, 2368–2375.
(16) Zhang, W.; Yang, Z.; Liu, Y.; Tang, S.; Han, X.; Chen, M. *J. Cryst. Growth* **2004**, *263*, 394–399.
(17) Zhang, Y.; Liu, Y.; Guo, F.; Hu, Y.; Liu, X.; Qian, Y. *Solid State Commun.* **2005**, *134*, 523–527.
(18) Xi, G.; Peng, Y.; Zhu, Y.; Xu, L.; Zhang, W.; Yu, W.; Qian, Y. *Mater. Res. Bull.* **2004**, *39*, 1641–1648.
(19) Sun, X.; Ma, C.; Wang, Y.; Li, H. *Inorg. Chem. Commun.* **2002**, *5*, 747–750.
(20) Zhou, F.; Zhao, X.; Yuan, C.; Xu, H. *J. Meter. Sci.* **2007**, *42*, 9978–9982.

Published on Web 05/22/2009

having an anisotropic morphology.[21] In addition, the fact that adsorption and redox reactions usually take place at solid/gas or solid/liquid interfaces[3−9] implies that improved performance may follow from an increased surface-to-volume ratio of nanometer-sized γ−MnOOH particles. The synthesis of γ−MnOOH nanowires/nanorods has already been widely reported.[12−20] For example, γ−MnOOH nanowires are achieved by reacting MnO_2 powders under hydrothermal conditions.[12−14] Folch et al. synthesized γ−MnOOH nanorods by a cluster growth route from $[Mn_{12}O_{12}(RCOO)_{16}(H_2O)_n]$ (R = CH_3 or C_2H_5).[15] Furthermore, hydrothermal reaction of $KMnO_4$ with reductants such as ethanol,[16] NH_4Cl,[17] and KI,[18] provides γ−MnOOH nanorods. Hydrothermal synthesis of γ−MnOOH nanowires/nanorods is also notably obtained via oxidation of Mn^{2+} ions with the presence of different organic compounds such as cetyltrimethylammonium bromide,[19] polyethylene glycol,[20] and tetraethyl ammonium hydroxide.[22] Despite the remarkable progress on the synthesis of γ−MnOOH nanowires/nanorods, few systematic studies focus so far on their size-dependent properties.[15]

The structural stability of γ−MnOOH nanowires/nanorods is of particular interest. On the one hand, the small crystal sizes of nanomaterials usually entail the danger of structural instability at elevated temperatures where diffusion of atoms becomes dominant.[23,24] On the other hand, thermal decomposition of γ−MnOOH is known to give distinct products dependent on the conditions.[25−29] For example, heating in air yields typically β−MnO_2, which further transforms to α−Mn_2O_3 and finally to Mn_3O_4 (i.e., $Mn^{2+}Mn_2^{3+}O_4$) through successive heating.[12−15,20,25] However, annealing in nitrogen or argon at intermediate temperatures (400 °C < T < 500 °C) is reported to produce Mn_3O_4 directly;[15,26] whereas heating in vacuum at 200−250 °C results in γ−Mn_2O_3 (i.e., $Mn^{3+}[Mn_{5/3}^{3+}\square_{1/3}]O_4$, □: vacancy), which decomposes into a mixture of Mn_3O_4 and Mn_5O_8 (i.e., $Mn_2^{2+}Mn_3^{4+}O_8$) upon further heating.[27] In addition, formation of Mn_5O_8 from γ−MnOOH in air at 300−400 °C has been reported.[25,29] It is still not very clear why and how the decomposition of γ−MnOOH upon heating can follow several paths. Apparently, thermodynamical and/or kinetic parameters play important roles in these structural reorganizations; however, the detailed microscopic mechanisms are not well understood.

The present work has two aims: to study the structural characteristics of recently discovered γ−MnOOH nanorods with small sizes and large amounts of active surface atoms; and to investigate their presumably size-dependent thermal behaviors. The γ−MnOOH nanorods are prepared by reacting $KMnO_4$ and ethanol under hydrothermal conditions and characterized by X-ray diffraction (XRD), transmission electron microscopy (TEM), Raman scattering, and X-ray photoelectron spectroscopy (XPS). Phase transitions of the as-prepared γ−MnOOH nanorods at elevated temperatures are monitored by means of in situ time-resolved synchrotron XRD, identifying also formation of possible intermediate phases.[25,28] To our knowledge, no such systematic studies using in situ XRD are so far reported.

Experimental Section

Hydrothermal Synthesis of γ−MnOOH Nanorods. γ−MnOOH nanorods were obtained by slightly modifying the procedure in ref 16. For a typical synthesis, 3 mL of absolute ethanol was added into 47 mL of aqueous solution of $KMnO_4$ (0.1 M) under vigorous stirring at room temperature. The obtained mixture was transferred into Teflon-lined stainless steel autoclaves, sealed and heated at 140 °C for 24 h without shaking or stirring during the heating. After the reaction, the autoclaves were cooled rapidly down to room temperature by means of tap water. The light brown precipitates of γ−MnOOH nanorods were filtered off, washed with distilled water, and dried at 80 °C overnight.

X-ray Photoelectron Spectroscopy (XPS). A small amount (∼ 50 mg) of the as-prepared materials was pressed into pellets (diameter: ∼0.6 mm; thickness: ∼1 mm), which were attached to the XPS sample holder via conductive carbon glue. XPS spectra were collected with a KRATOS Axis Ultra-DLD spectrometer under monochromatic Al Kα radiation (1486.6 eV). A pass energy of 80 eV with a step size of 1 eV was used for survey scans. For separate photoelectron lines, a pass energy of 20 eV was used with a step size of 0.1 eV. The surfaces of the samples were flooded with low-energy electrons to compensate for electrostatic charging. Energy referencing was based on the C−C component of the C(1s) at 285.0 eV. All samples were studied at room temperature at a pressure of approximately 10^{-8} Torr.

Raman Scattering Spectroscopy. Spectra with resolution of about 2 cm^{-1} were collected in a backscattering configuration at room temperature with 30−60 s recording time. The samples were illuminated by a 632.8 nm He−Ne laser on an Olympus BX 40 confocal microscope with a 10× objective. Wavenumber stability and instrumental accuracy were calibrated by recording the F_{2g} Raman-active mode of silicon at 521 cm^{-1}. A laser power of 1 mW was used, low enough to prevent damage.

Powder X-ray Diffraction (XRD). Phase analysis was based on powder X-ray diffraction (XRD) data collected on a Siemens D5000 powder diffractometer (Cu $K\alpha_1$ radiation λ = 0.15406 nm; PSD detector; reflection geometry). In situ time-resolved synchrotron XRD data were collected in transmission mode (λ = 0.7107 Å) at the Swiss-Norwegian Beamline (BM01A) at the European Synchrotron Radiation Facility (ESRF), Grenoble. The samples were loaded into a 0.7 mm quartz-glass capillary and thereafter mounted in a swagelok fitting. Temperature and atmosphere were controlled during heating. Data were collected every 2 min. Selected synchrotron XRD patterns were analyzed by the Rietveld method using GSAS[30] and EXPGUI[31] softwares (see Supporting Information).

Characterization. Morphology and composition of the samples were analyzed by scanning electron microscopy (SEM, FEI Quanta 200F) and transmission electron microscopy (TEM, Philips CM30ST) equipped with an energy-dispersive X-ray spectrometer (EDX). Image processing was done with Digital Micrograph (Gatan).

(21) Patzke, G. R.; Krumeich, F.; Nesper, R. *Angew. Chem., Int. Ed.* **2002**, *41*, 2446–2461.
(22) Sharma, P. K.; Whittingham, M. S. *Mater. Lett.* **2001**, *48*, 319–323.
(23) Hui, L.; Pederiva, F.; Wang, B. L.; Wang, J. L.; Wang, G. H. *Appl. Phys. Lett.* **2005**, *86*, 011913 (3 pages).
(24) Kamins, T. I.; Li, X.; Williams, R. S. *Appl. Phys. Lett.* **2003**, *82*, 263–265.
(25) Rask, J. H.; Buseck, P. R. *Am. Mineral.* **1986**, *71*, 805–814.
(26) Yang, Z.; Zhang, Y.; Zhang, W.; Wang, X.; Qian, Y.; Wen, X.; Yang, S. *J. Solid State Chem.* **2006**, *179*, 679–684.
(27) Hernann, L.; Morales, J.; Tirano, J. L. *Surf. Coat. Technol.* **1986**, *27*, 343–350.
(28) Fritsch, S.; Sarrias, J.; Rousset, A.; Kulkarni, G. U. *Mater. Res. Bull.* **1998**, *33*, 1185–1194.
(29) Oswald, H. R.; Feitknecht, W.; Wampetich, M. J. *Nature* **1965**, *207*, 72.
(30) Larson, A. C.; Von Dreele, R. B. *Los Alamos National Laboratory Report LAUR* **1994**, 86–748.
(31) Toby, B. H. *J. Appl. Crystallogr.* **2001**, *34*, 210–213.

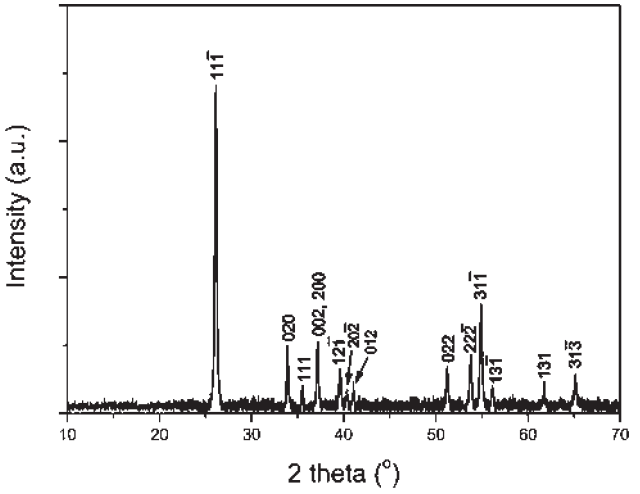

Figure 1. Powder XRD pattern of the as-synthesized materials (λ = 1.540598 Å). Miller indices included.

Results and Discussion

Growth of γ−MnOOH Nanorods. Light brown solid materials were obtained by autoclaving $KMnO_4$ aqueous solutions at 140 °C in the presence of ethanol. The as-prepared products were characterized by powder XRD (Figure 1). All observed reflections are perfectly indexed on the monoclinic unit cell for γ−MnOOH with parameters a = 5.300 Å, b = 5.278 Å, c = 5.307 Å, and β = 114.36° (JCPDS 41−1379).[32] It reveals clearly that single-phase γ−MnOOH materials have been obtained. As shown in Figure 1, the diffraction peaks are relatively sharp and intense, indicating that the as-prepared γ−MnOOH materials are well crystallized.

The morphology of as-synthesized γ−MnOOH was analyzed by SEM. Figure 2a demonstrates a large quantity of rod-like nanostructures. The fibrous morphology of the products suggests an anisotropic growth behavior under present experimental conditions. Detailed SEM observations reveal that the nanorods have typical diameters ranging from 20 to 500 nm and lengths from hundreds of nanometers to a few micrometers, respectively. The individual γ−MnOOH nanorods are considered as dense and appear to have uniform diameter throughout their entire lengths (Figure 2b). Compositional analysis (inset of Figure 2b) confirms that the nanorods are composed of O and Mn (H not detectable by EDX). For some materials the presence of trace amount of K is observed (not shown here), probably because of the residues of reactants or products.

More details on the microstructures of as-prepared γ−MnOOH nanorods were obtained from TEM, see Figure 3. The individual γ−MnOOH nanorods are structurally uniform. The typical electron diffraction patterns (inset of Figure 3a) indicate single crystalline rods with axis along the crystallographic ⟨101⟩. The crystal lattice is nicely imaged in the high-resolution TEM pictures (Figure 3b). The measured distance, 0.34 nm, between lines parallel to the rod axis corresponds to the interplanar spacing of (−111); the 0.28 nm interplanar distance corresponds to (101) perpendicular to the rod axis.

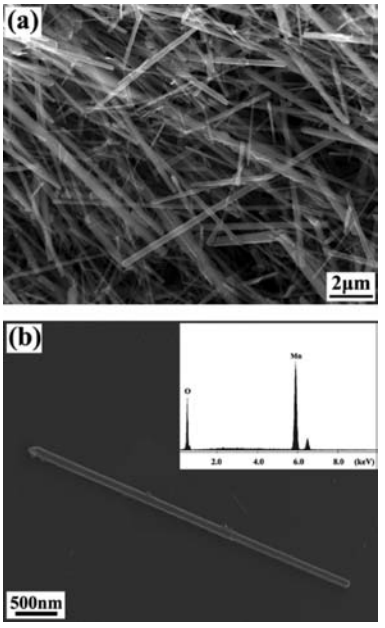

Figure 2. SEM images of the as-prepared γ−MnOOH nanorods. Inset of (b) shows a typical EDX spectrum of the nanorods.

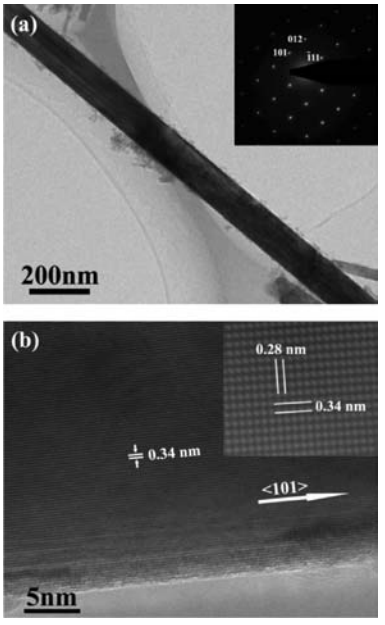

Figure 3. Typical TEM images of as-prepared γ−MnOOH nanorods. Inset to panel (a) shows the electron diffraction pattern along [1, 2, −1]. Inset to panel (b) shows a Fourier-filtered lattice image. The measured distances, 0.28 and 0.34 nm, correspond to the interplanar spacing of (1 0 1) and (−1 1 1) plane, respectively.

The ⟨101⟩ is unambiguously the growth direction of the current γ−MnOOH nanorods. Note that γ−MnOOH is a tunnel-structured compound with interstitial (1 × 1) tunnels along the ⟨101⟩ of the monoclinic unit-cell.[2,32] This correlates with the fast crystal growth observed along the tunnel direction, which is in line with observations for tunnel-structured Mn oxides.[33,34]

(32) Kohler, T.; Armbruster, T.; Libowitzky, E. *J. Solid State Chem.* **1997**, *133*, 486–500.

(33) Gao, T.; Glerup, M.; Krumeich, F.; Nesper, R.; Fjellvåg, H.; Norby, P. *J. Phys. Chem. C* **2008**, *112*, 13134–13140.

(34) Shen, X. F.; Ding, Y. S.; Hanson, J. C.; Aindow, M.; Suib, S. L. *J. Am. Chem. Soc.* **2006**, *128*, 4570–4571.

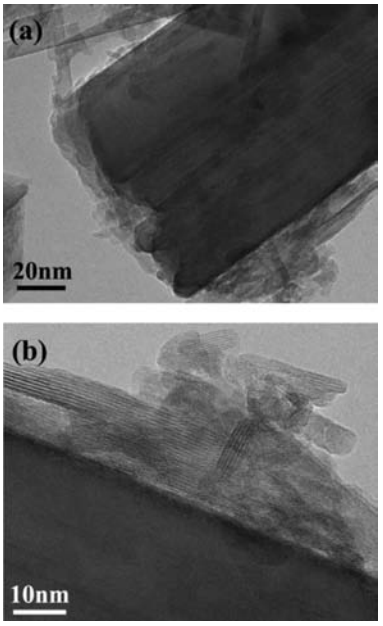

Figure 4. (a) TEM image of a thick γ−MnOOH fiber consisting of several smaller ones. (b) An enlargement shows the small elongated crystalline particles on the surfaces of the γ−MnOOH nanorods.

As shown in Figure 4a, the thicker γ−MnOOH nanorods consist usually of bundles of smaller rods that aggregate along the rod axis direction. Moreover, the presence of elongated γ−MnOOH particles on the surface of the thick rods is noticeable (Figure 4b). These are typical features for the self-assembly growth of Mn oxide nanorods from solutions.[35] As mineral, γ−MnOOH is usually formed by oxidization of Mn^{2+} ions in aquatic environments.[1,36] Alkaline conditions are necessary since the materials dissolve for a pH below 6.[37] In the current reaction MnO_4^- is reduced by ethanol to produce Mn^{3+} and OH^- that precipitates into γ−MnOOH:

$$KMnO_4(aq) + 2CH_3CH_2OH(aq) \rightarrow MnOOH(s) + 2CH_3CHO(aq) + KOH(aq) + H_2O \quad (1)$$

The primary γ−MnOOH particles produced should have an elongated, rod-like morphology thanks to their anisotropic growth behavior; subsequently, these primary rods would aggregate along the rod axis direction to form a thick rod via lateral attachment (Figure 4). The present observation is similar to that previously observed in cryptomelane-type MnO_2 nanorods.[33,35]

Surface Properties of γ−MnOOH Nanorods. The XPS results in Figure 5 show photoelectron peaks of Mn, O, C, and K; and the Auger peaks of Mn *LMM* and O *KLL*. The dominating peaks corresponds to O(1s), Mn($2p_{3/2}$) and Mn($2p_{1/2}$) at binding energies 530, 641, and 653 eV, respectively. The presence of K(2s) and C(1s) photoelectron peaks can be noted. The K signal represents most likely surface contaminations from the synthesis medium (e.g., Reaction 1).

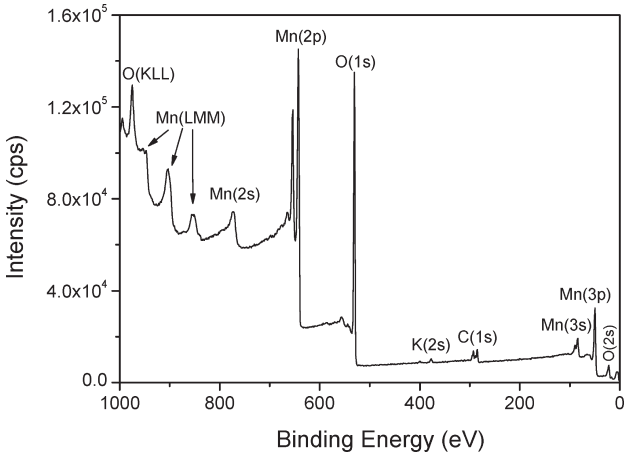

Figure 5. XPS spectrum of the as-prepared γ−MnOOH nanorods.

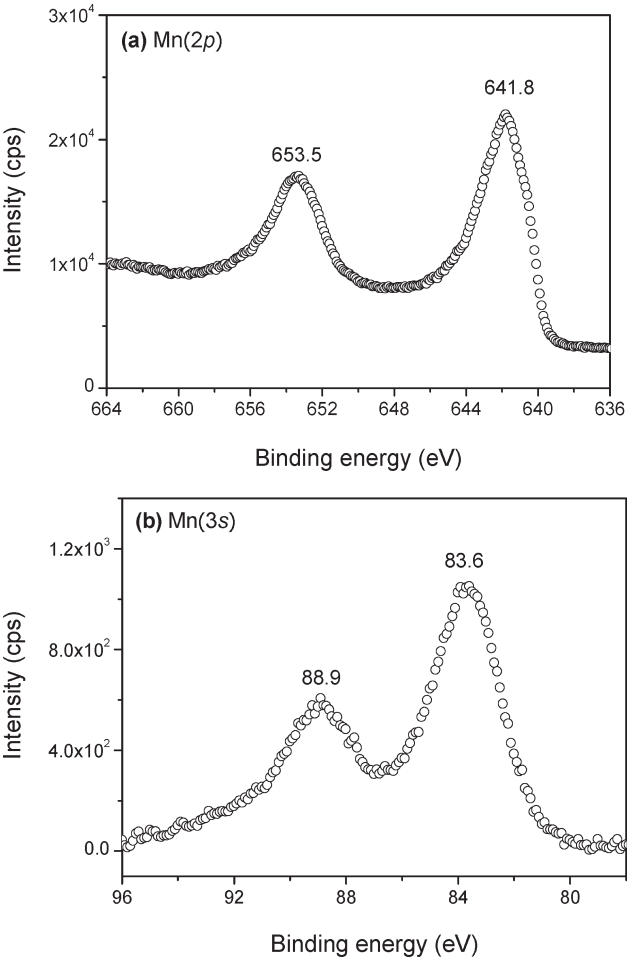

Figure 6. XPS spectra of the (a) Mn(2p) and (b) Mn(3s) region of the as-prepared γ−MnOOH nanorods.

The multiplet splitting of the observed Mn(2p) and Mn(3s) core-level peaks are reported in Figure 6. The Mn($2p_{3/2}$) peak is asymmetric toward higher binding energy, whereas the Mn($2p_{1/2}$) is asymmetric toward lower binding energy, which is characteristic for 3*d* metals with unpaired electrons in outer valence shell.[38−40]

(35) Portehault, D.; Cassaignon, S.; Baudrin, E.; Jolivet, J. P. *Chem. Mater*. **2007**, *19*, 5410–5417.
(36) Moore, T. E.; Ellis, M.; Selwood, P. W. *J. Am. Chem. Soc*. **1950**, *72*, 856–866.
(37) Ramstedt, M.; Andersson, B.; Shchukarev, A.; Sjöberg, S. *Langmuir* **2004**, *20*, 8224–8229.
(38) Fadley, C. S.; Shirley, D. A. *Phys. Rev. A* **1970**, *2*, 1109–1120.
(39) Kowalczyk, S. P.; Ley, L.; McFeely, F. R.; Shirley, D. A. *Phys. Rev. B* **1975**, *11*, 1721–1727.
(40) Carver, J. C.; Schweitzer, G. K. *J. Chem. Phys*. **1972**, *57*, 973–982.

Table 1. $Mn(2p_{3/2})$ Binding Energy and the Mn(3s) Splitting Data for Trivalent Mn Ions

compounds	$Mn(2p_{3/2})$ (eV)[a]	Mn(3s) splitting (eV)	ref.
$\gamma-MnOOH$	641.7; 641.8; 641.7	5.5; - ; 5.3	42; 41; 44
	641.8	5.3	this work
Mn_2O_3	641.8; 641.8	5.4; 5.4	40; 39

[a] Estimated experimental error ± 0.2 eV.

The observed binding energies for the $Mn(2p_{3/2})$ and $Mn(2p_{1/2})$ satellites for the $\gamma-MnOOH$ nanorods are in good agreement with data on $\gamma-MnOOH$ or Mn_2O_3 (Table 1).[41−43] The multiplet splitting of the Mn(3s) peak is very convenient for identifying the oxidation states of Mn.[44,45] This splitting occurs when the 3s electron is photoejected from a paramagnetic atom; the remaining 3s electron couples with the valence 3*d* electron, giving rise to parallel or antiparallel spin configuration. Therefore two photoelectron peaks appear. The magnitude of the splitting energy increases as the Mn oxidation state decreases.[44] The Mn(3s) multiplet splitting energy for the current $\gamma-MnOOH$ nanorods is 5.3 eV, in excellent agreement with literature data for $\gamma-MnOOH$ and Mn_2O_3 (Table 1).[45] This should be compared with the smaller Mn(3s) splitting energy of 4.6 eV, typical for tetravalent Mn (see Supporting Information).[46,47] Considering a typical penetration depth of a few atomic layers for the XPS probe, the observed spectra show no indication for any surface oxidation of the $\gamma-MnOOH$ nanorods.

The O(1s) spectrum in Figure 7 has its maximum near 530 eV and a distinct shoulder with a pronounced tail on the high energy side of the peak. The separations, relative intensities, and widths of the O(1s) peaks as deconvoluted by Gaussian fits are listed in Table 2. There appear to be at least three spectral contributions. The ideal $\gamma-MnOOH$ has equal abundance of O^{2-} (oxygen that bonds solely to Mn^{3+}) and OH^- (oxygen that also bonds to hydrogen), and hence equal contributions of these species to the O(1s) spectrum. Any physisorbed and chemisorbed H_2O is expected to give another contribution to the observed O(1s) spectrum. Nesbitt and Banerjee found that the oxide O^{2-}, hydroxide OH^-, and water H_2O peaks were located at 529.6, 530.8, and 532.3 eV, respectively.[42] Ramstedt reported the similarly three overlapping O(1s) peaks in the XPS spectrum of $\gamma-MnOOH$,[48] at 530.2, 531.5, and 533.5 eV. In this work (Table 2), we hence assign the deconvoluted peaks at 530.0, 531.2, and 532.3 eV to O^{2-}, OH^-, and H_2O species, respectively.

The O^{2-} and OH^- peaks (Figure 7) show different intensities and fwhm values (Table 2). The oxide O^{2-} contribution is much higher than the hydroxide

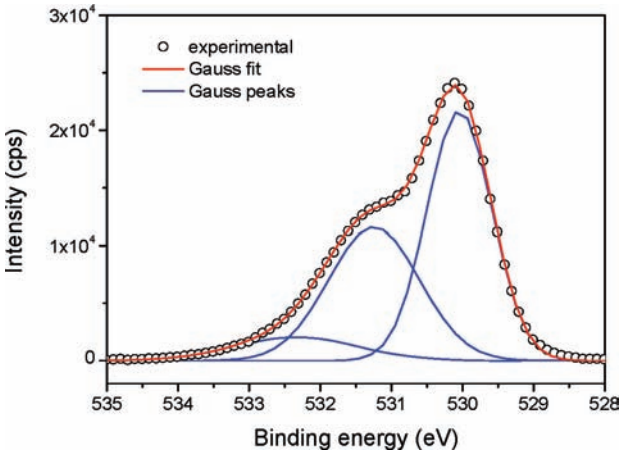

Figure 7. O(1s) XPS spectrum of the as-prepared $\gamma-MnOOH$ nanorods.

Table 2. O(1s) Multiplet Branching Ratios for $\gamma-MnOOH$ Nanorods

	name	binding energy (eV)[a]	fwhm[b] (eV)	area	percentage[c] (%)
O(1s)	O^{2-}	530.0	0.9	24829.3	51.9
	OH^-	531.2	1.2	18621.0	38.9
	H_2O	532.3	1.7	4391.7	9.2

[a] Estimated experimental error ± 0.2 eV. [b] All peaks are modeled as 100% Gaussian. [c] The percentage represents the contribution of each peak to the total number of counts under the O(1s) peak.

OH^- peak, indicating hydrogen deficiency in the near-surface region of the $\gamma-MnOOH$ nanorods. This is remarkably distinctive from previous reports on $\gamma-MnOOH$.[42,48] Since tetravalent Mn ions are unlikely (see Figure 6 and Table 1), the negative surface charges due to hydrogen deficit may possibly be compensated by surface complexes with K^+ ions or hydrocarbons from the reaction medium (see Reaction 1). The $\gamma-MnOOH$ nanorods have small crystal sizes and consequently large amounts of surface atoms that are chemically active. Hence, the formation of surface complexes between K^+ ions or hydrocarbons from the reaction medium and these active surface atoms would be possible. This may explain the presence of K(2s) and C(1s) photoelectron peaks in Figure 5. As a consequence, one might expect somewhat different surface properties of the present $\gamma-MnOOH$ nanorods compared with those reported previously.[37,42,48] Further study along this line is of interest for the details.

Topotactic Conversion of $\gamma-MnOOH$ to $\beta-MnO_2$. The structural evolutions of the as-prepared $\gamma-MnOOH$ nanorods were followed by in situ synchrotron XRD upon heating in air. As seen in Figure 8, monoclinic $\gamma-MnOOH$ transforms into tetragonal $\beta-MnO_2$ upon heating at about 200 °C. Moreover, there exists an intermediate phase during the transformation, as indicated by arrows in Figure 8. This structure is identified by the three reflections at $d = 3.54$ Å, $d = 2.49$ Å, and $d = 1.59$ Å. The intermediate totally disappears as the transformation to $\beta-MnO_2$ is complete.

The synchrotron XRD data of $\gamma-MnOOH$ and $\beta-MnO_2$ were analyzed according to the Rietveld method to ascertain structural aspects of the nanomaterials

(41) Stranick, M. A. *Surf. Sci. Spectra* **1999**, *6*, 39–46.
(42) Nesbitt, H. W.; Banerjee, D. *Am. Mineral.* **1998**, *83*, 305–315.
(43) Ardizzone, S.; Bianchi, C. L.; Tirelli, D. *Colloids Surf. A* **1998**, *134*, 305–312.
(44) Galakhov, V. R.; Demeter, M.; Bartkowski, S.; Neumann, M.; Ovechkina, N. A.; Kurmaev, E. Z.; Lobachevskaya, N. I.; Mukovskii, Ya. M.; Mitchell, J.; Ederer, D. L. *Phys. Rev. B* **2002**, *65*, 113102 (4 pages).
(45) Murray, J. W.; Dillard, J. G.; Giovanoli, R.; Moers, H.; Stumm, W. *Geochim. Cosmochim. Acta* **1985**, *49*, 463–470.
(46) Stranick, M. A. *Surf. Sci. Spectra* **1999**, *6*, 31–38.
(47) Allen, G. C.; Harris, S. J.; Jutson, J. A.; Dyke, J. M. *Appl. Surf. Sci.* **1989**, *37*, 111–134.
(48) Ramstedt, M.; Shchukarev, A.; Sjöberg, S. *Surf. Interface Anal.* **2002**, *34*, 632–636.

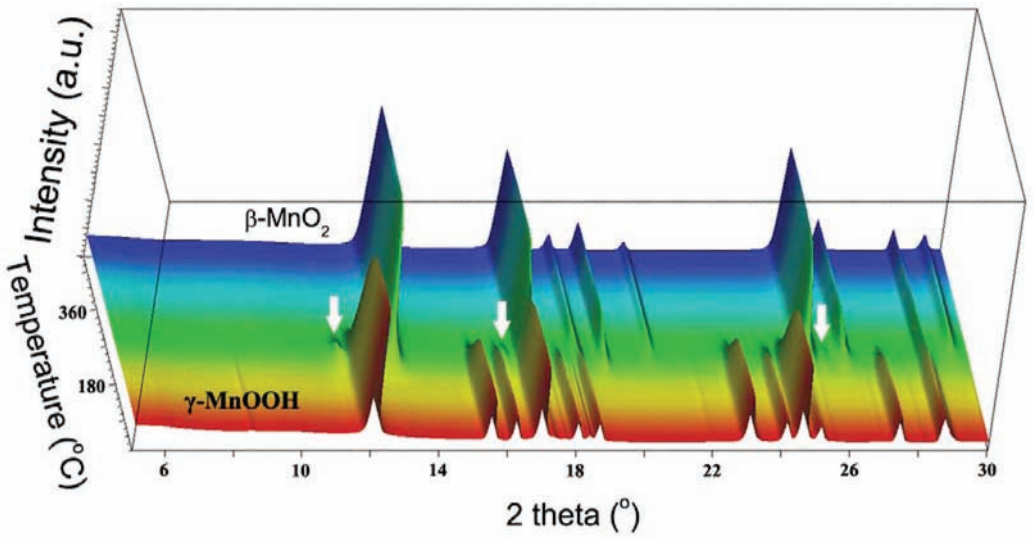

Figure 8. In situ time-resolved synchrotron XRD patterns (λ = 0.7107 Å) for the as-prepared $\gamma-$MnOOH nanorods heated in air. Arrows show an intermediate phase.

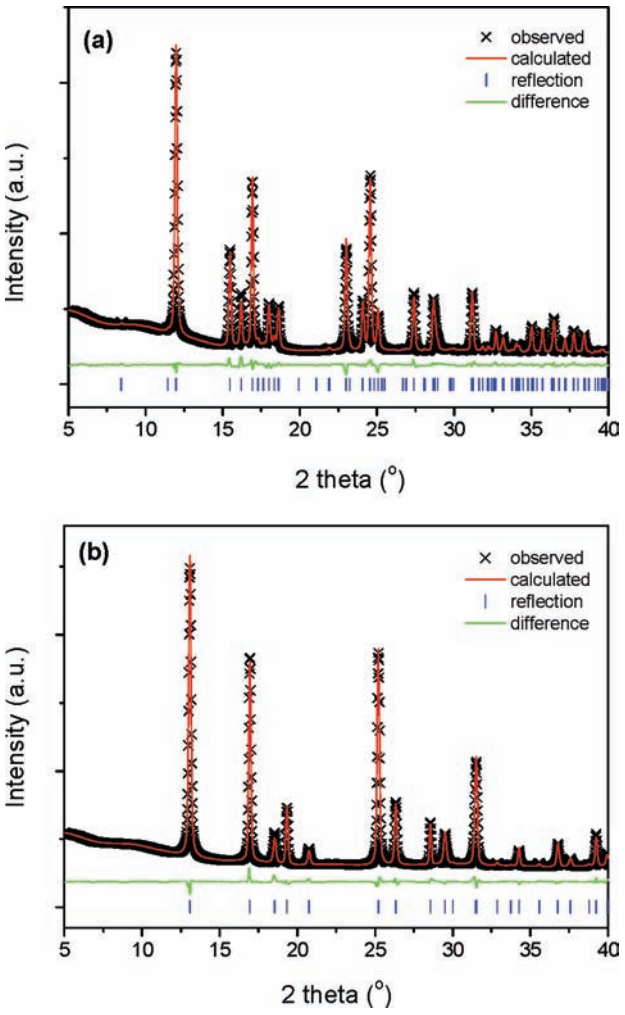

Figure 9. Results from Rietveld refinement on synchrotron XRD data of (a) $\gamma-$MnOOH and (b) $\beta-MnO_2$ nanorods (λ = 0.6998 Å).

during the thermal transformation. The observed, calculated, and difference patterns are shown in Figure 9. The unit cell dimensions for the as-prepared $\gamma-$MnOOH nanorods a = 5.2983(3) Å, b = 5.2782(2) Å, c = 5.3067(3) Å, and β = 114.401(2)°, are in good agreement with published values.[32,49] Moreover, $\beta-MnO_2$ crystallizes into a tetragonal structure (space group $P4_2/mnm$, No. 136) with unit cell dimensions a = 4.39629(7) Å and c = 2.87132(4) Å.[50] Selected interatomic distances are reported in Table 3.

Table 3. Selected Interatomic Distances (Å) in MnO_6 Octahedron in $\gamma-$MnOOH and $\beta-MnO_2$ Nanofibers[a]

	$\gamma-$MnOOH		
Mn−O1	1.971(13)	Mn−O2	1.893(15)
Mn−O1	2.015(11)	Mn−O2	1.898(11)
Mn−O1	2.325(9)	Mn−O2	2.215(9)
	$\beta-MnO_2$		
Mn−O1	1.8885(11) × 2	Mn−O1	1.8841(7) × 4

[a] Calculated standard deviations are in parentheses.

Figure 10 compares the crystal structures of $\gamma-$MnOOH and $\beta-MnO_2$. They are structurally related with (1 × 1) tunnels built by single chain of edge-sharing MnO_6 octahedra. In $\gamma-$MnOOH, the Mn atoms of the Jahn−Teller deformed MnO_6 octahedron form four short and two long Mn−O bonds (Table 3). The hydrogen is located in the interstitial (1 × 1) channels and bonds to O1 and O2, forming OH groups.[32,49] Upon heating, hydrogen is removed from the channels (Figure 10) during the $\gamma-$MnOOH to $\beta-MnO_2$ transformation. Apparently, the $\gamma-$MnOOH → $\beta-MnO_2$ transformation is isomorphic, which is confirmed by TEM analyses reported in Figure 11. The resulting $\beta-MnO_2$ materials inherit the same rod-like morphology as the $\gamma-$MnOOH nanorod precursors (Figure 11a).[12,19,20] Moreover, the obtained $\beta-MnO_2$ nanorods are single crystalline, as evidenced by electron diffraction data (inset of Figure 11a). High-resolution TEM data (Figure 11b) reveal that the $\beta-MnO_2$ nanorods are elongated along [001], that is, the (1 × 1) tunnel direction (see Figure 10).

Previous study revealed that migration of H out of the structure is triggering the topotactic $\gamma-$MnOOH→$\beta-MnO_2$

(49) Buerger, M. J. *Z. Kristallogr.* **1936**, *95*, 163–174.
(50) Bolzan, A. A.; Fong, C.; Kennedy, B. J.; Howard, C. J. *Aust. J. Chem.* **1993**, *46*, 939–944.

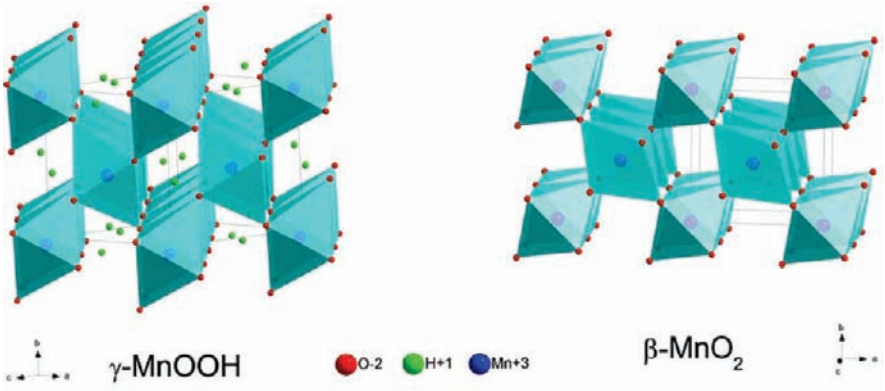

Figure 10. Polyhedral representation of the crystal structure of $\gamma-MnOOH$ and $\beta-MnO_2$. Solid lines show the unit cells.

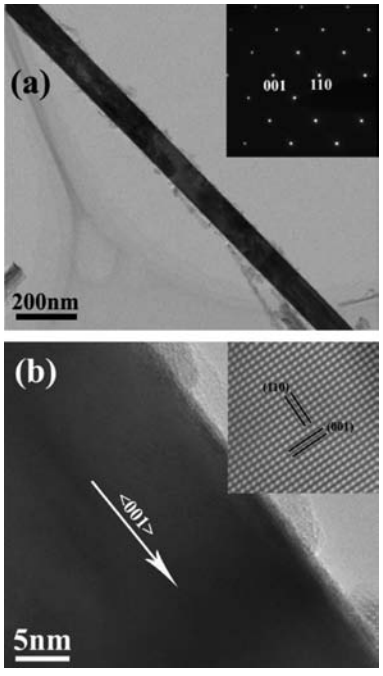

Figure 11. Typical TEM images of the $\beta-MnO_2$ nanorods produced by heating the $\gamma-MnOOH$ nanorod precursors in air at 300 °C for 2 h. Inset of panel (a) shows an electron diffraction pattern. Inset of panel (b) shows an enlarged two-dimensional lattice image (Fourier filtered), in which the measured distances correspond to the interplanar spacing of (1 1 0) and (0 0 1) plane, respectively.

transformation rather than the influx of oxygen:[25]

$$4\gamma-MnOOH(s) + O_2(g) \rightarrow 4\beta-MnO_2(s) + 2H_2O \quad (2)$$

The Jahn−Teller distorted MnO_6 octahedron in $\gamma-MnOOH$ converts to a quite regular MnO_6 octahedron in $\beta-MnO_2$ (Table 3). The two long Mn−O bonds in $\gamma-MnOOH$ decrease strongly (18.9% and 14.9%, respectively) upon converting to $\beta-MnO_2$, which relates to the 16.7% contraction of the *b* axis during the transformation (from 5.2782 Å to 4.3963 Å). This contraction usually generates local strain[25,51] and has been found to cause lamellar pores in the resulted $\beta-MnO_2$.[52,53] This appears, however, to be negligible for the nanorods, as demonstrated by the structural studies above. For example, the present $\beta-MnO_2$ nanorods are well crystallized (Figure 11) with no indications of lamellar pores or other defects that could release the local strain. This significant difference reveals that local structural evolutions of $\gamma-MnOOH$ nanorods at elevated temperatures are caused mainly by kinetics. The $\gamma-MnOOH$ nanorods with small crystallite sizes may readily accommodate the volume changes during the transitions,[54] preserving their rod-like morphology. This conclusion seems also applicable to the $\beta-MnO_2 \rightarrow Mn_2O_3$ nanorod transition.[12,20]

The $\gamma-MnOOH \rightarrow \beta-MnO_2$ transformation takes place at about 200 °C for the nanorods, while at about 300−350 °C for bulk materials.[25,32,52] Smaller nanoparticles with larger surface-to-volume ratio usually exhibit higher surface energy; therefore, they require less enthalpy for lattice distortions, resulting in decreased phase transition temperatures.[23,24] Moreover, with the decrease of the particle sizes, the ratio of the number of surface atoms to the total number of atoms increases rapidly. These atoms are in general chemically active and possess high diffusion mobility at elevated temperatures. This feature will be particular useful for the synthesis of other complex Mn oxides[9−11] on the basis of $\gamma-MnOOH$ nanorod precursors.

Intermediate Phase. The intermediate phase that forms during the transformation from $\gamma-MnOOH$ to $\beta-MnO_2$ (Figure 8) exists only for a short time/temperature interval during the in situ heating experiments. This suggests that the intermediate is metastable and governed by kinetics. The time/temperature evolution of the diffraction peaks from $\gamma-MnOOH$, the intermediate, and $\beta-MnO_2$ is shown in Figure 12 for the $\gamma-MnOOH \rightarrow \beta-MnO_2$ transformation. The intensity of the (11−1) reflection of the monoclinic $\gamma-MnOOH$ is observed to decline smoothly along with the increase of temperature; moreover, the reflection attributed to (110) of tetragonal $\beta-MnO_2$ begins to appear in the diffraction patterns, and its intensity increases smoothly. Concomitant with this, the intensities of the reflections corresponding to the intermediate phase increase gradually, reach a maximum, and then decline smoothly and totally disappear as the $\gamma-MnOOH \rightarrow \beta-MnO_2$ transition is complete. This suggests that the intermediate phase could show close structural resemblance to the involved tunnel structures.

(51) de Wolff, P. M. *Acta Crystallogr.* **1959**, *12*, 341–345.
(52) Champness, P. E. *Mineral. Mag.* **1971**, *38*, 245–248.
(53) Yamada, N.; Ohmasa, M.; Horiuchi, S. *Acta Crystallogr. B* **1986**, *42*, 58–61.
(54) Jiao, F.; Bruce, P. G. *Adv. Mater.* **2007**, *19*, 657–660.

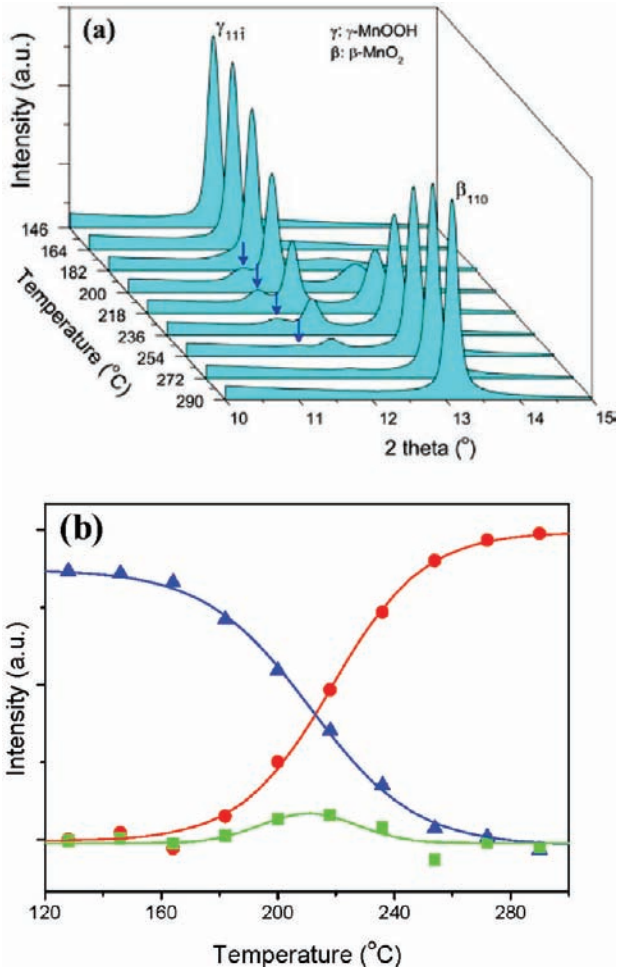

Figure 12. (a) 3D plot of selected in situ time-resolved synchrotron XRD patterns near the transition temperature for the as-prepared $\gamma-$MnOOH nanorods heated in air. Arrows indicate the intermediate structure ($\lambda = 0.7107$ Å). (b) 2D plot showing the decline in intensity with temperature of the $\gamma-$MnOOH (11−1) reflection (blue triangles) and the growth of $\beta-MnO_2$ (110) reflection (red circles); the variation of the reflection $d = 3.54$ Å (green squares) of the metastable, intermediate phase is included for comparison. The estimated errors for the data points are < 5%. Solid curves are drawn in only to guide the eye.

Note that the (110) plane of the monoclinic $\gamma-$MnOOH involves only O atoms and has a d value of about 3.56 Å. It is reasonable to attribute this metastable structure to the hydrogen evolution within the (1 × 1) channels.

Previously, Rask and Buseck have reported on a Mn-oxide with weak reflections corresponding to a periodicity of $d = 7.2$ Å on the basis of high-resolution TEM studies; and suggesting ordering of OH groups or Mn atoms with different oxidization states across the (101) plane of $\beta-MnO_2$.[25] The present observation of a strong peak at $d = 3.54$ Å for the intermediate phase matches fairly well to half the spacing $d = 7.2$ Å. Possibly, the new Mn-oxide reported by Rask and Buseck might be the same as the intermediate phase observed currently. One might under high-energy electron beam irradiation foresee the possibility of $\gamma-$MnOOH being partially dehydrated, and forming the mentioned intermediate structure. If so, the previous assignment of this structure to $\beta-MnO_2$[25] will be no longer valid.

Raman Scattering Study. Figure 13a shows a representative Raman scattering spectrum of the as-prepared

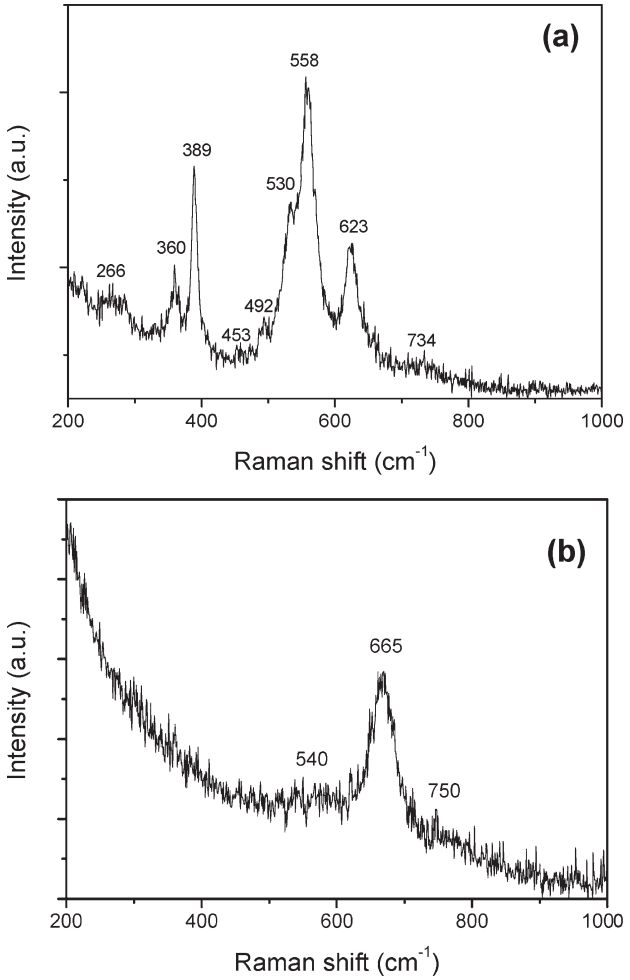

Figure 13. Raman scattering spectra of (a) $\gamma-$MnOOH and (b) $\beta-MnO_2$ nanorods.

$\gamma-$MnOOH nanorods. At least nine Raman modes are clearly observed. Among them, five main well-defined contributions at 360, 389, 530, 558, and 623 cm^{-1} reflect good crystallinity and match very well to the previous study on $\gamma-$MnOOH.[55] Figure 13b shows the Raman scattering spectrum of tetragonal $\beta-MnO_2$, which is prepared by heating the $\gamma-$MnOOH nanorods in air at 300 °C (see Supporting Information). The modes observed are in good agreement with literature data for $\beta-MnO_2$.[56]

As confirmed by the XRD studies (see above), $\gamma-$MnOOH crystallizes in the monoclinic C_{2h}^5-$P2_1/c$ space group. The unit cell contains four MnOOH formula units. All atoms occupy general positions (Wyckoff site 4*e*) with site symmetry C_1. The correlation between the C_1 site group and the C_{2h} factor group yields 45 optical phonons (after subtracting the $K = 0$ acoustic modes) of symmetry 12 A_g + 11 A_u + 12 B_g + 10 B_u. Of these, all *gerade* modes are Raman active. In practice, not all predicted Raman-active modes (12 A_g + 12 B_g) are observed for polycrystalline samples because of low polarizabilities as well as spectral overlap of modes.

(55) Bernard, M. C.; Goff, A. H.; Thi, B. V.; de Torresi, S. C. *J. Electrochem. Soc.* **1993**, *140*, 3065–3070.
(56) Gao, T.; Fjellvåg, H.; Norby, P. *Nanotechnology* **2009**, *20*, 055610 (7 pages).

Moreover, some of the Raman modes might have too little intensity to be observed.[33] Presently, at least nine Raman scattering bands are identified, Figure 13a, consistent with the low symmetry of the $\gamma-$MnOOH with monoclinic structure. A detailed assignment can not be given at this stage because spectra on oriented single crystal are not available. However, comparison with Raman scattering data of other Mn oxides (see Supporting Information) reveals that all observed modes can be attributed to monoclinic $\gamma-$MnOOH, primarily to Mn−O vibrations without significant contributions from the tunnel hydrogen.[57] For detailed Raman studies of $\gamma-$MnOOH nanorods, micro-Raman spectroscopy will enable measurement of single freestanding nanorods.[58] We expect to pursue these aspects in forthcoming studies.

Conclusions

Single crystalline $\gamma-$MnOOH nanorods have been prepared by reacting $KMnO_4$ and ethanol under hydrothermal conditions. The formed $\gamma-$MnOOH nanorods show lateral attachment to primary nanorods elongated along ⟨101⟩. XPS shows that the surface of the $\gamma-$MnOOH nanorods is hydrogen deficient and compensated by surface complexation. The $\gamma-$MnOOH nanorods have nine Raman bands at 266, 360, 389, 453, 492, 530, 558, 623, and 734 cm^{-1}. The monoclinic $\gamma-$MnOOH nanorods can transform into tetragonal $\beta-MnO_2$ through topotactic reaction, during which the formation of a metastable intermediate phase is identified that possibly involves OH ordering within (110) of the monoclinic $\gamma-$MnOOH nanorods.

Acknowledgment. The authors acknowledge the financial assistance from the Research Council of Norway through the NANOMAT program (163565-431). ESRF is gratefully acknowledged for beam time made available through proposal number CH-2140. TEM measurements of this work are performed at the EMEZ (electron microscopy ETH Zurich).

Supporting Information Available: In situ synchrotron XRD data, Rietveld refinement details, and XRD and Raman scattering spectra of some derived Mn oxides. This material is available free of charge via the Internet at http://pubs.acs.org.

(57) Gao, T.; Fjellvåg, H.; Norby, P. *Inorg. Chem.* **2009**, *48*, 1423–1432.
(58) Hsiao, C. L.; Tu, L. W.; Chi, T. W.; Chen, M.; Young, T. F.; Chia, C. T.; Chang, Y. M. *Appl. Phys. Lett.* **2007**, *90*, 043102 (3 pages).